Light Water Reactor Sustainability Program

Modeling Late Blooming Phase Evolution during Post-irradiation Annealing in Select Reactor Pressure Vessels: Milestone 2 Report

March 31, 2016

U.S. Department of Energy

Office of Nuclear Energy

Light Water Reactor Sustainability Program

Modeling Late Blooming Phase Evolution during Post-irradiation Annealing in Select Reactor Pressure Vessels: Milestone 2 Report

Shipeng Shu (University of Wisconsin–Madison)
Huibin Ke (University of Wisconsin–Madison)
Dane D. Morgan (University of Wisconsin–Madison)

Key Collaborators
G. Robert Odette (University of California, Santa Barbara)
Peter B. Wells (University of California, Santa Barbara)

March 31, 2016

Prepared for the
U.S. Department of Energy
Office of Nuclear Energy

SUMMARY

This report has been assembled to address a milestone of the Irradiation-Induced Phase Transformations in High-Fluence Core Internals Project, which was defined as M3LW-16OR0402052— Complete report detailing the refinement of models for radiation-induced Mn-Ni-Si precipitate formation kinetics against experimental thermal annealing data.

This work was done in close collaboration with Professor G. R. Odette and his group at the University of California, Santa Barbara, and in particular, Dr. Peter Wells. The regular and strong interactions between all the participants in this collaboration has been critical to the development of this work and the content here represents intellectual contributions from the entire team.

ACKNOWLEDGEMENTS

This research was sponsored by the United States Department of Energy, Office of Nuclear Energy, for the Light Water Reactor Sustainability Research and Development effort.

CONTENTS

FIGURES

TABLES

ACRONYMS AND NOMENCLATURE

APT	atom probe tomography
bcc	body-centered cubic
CD	cluster dynamics
CM6	Name of different alloy composition used by University of California, Santa Barbara, collaborators
LG	Name of different alloy composition used by University of California, Santa Barbara, collaborators
KMC	kinetic Monte Carlo
MNSP	Mn-Ni-Si rich precipitate
PIA	post-irradiation annealing
RIS	radiation-induced segregation
RMSD	root mean square difference
RPV	reactor pressure vessel

Modeling Late Blooming Phase Evolution during Post-irradiation Annealing in Select Reactor Pressure Vessels: Milestone 2 Report

1. INTRODUCTION

Reactor pressure vessels (RPVs) are a permanent component of light water reactors and their irradiation embrittlement is one of the potential barriers to extending the lifetime of light water reactors. Embrittlement of RPVs is caused mainly due to the formation of nanometer-scaled Cu-rich precipitates and Mn-Ni-Si rich precipitates (MNSPs).[1] It is well known that with the very low solubility of Cu in Fe at the reactor service temperature (~300°C), Cu-rich precipitates form at low to intermediate neutron fluence (ϕt) due to their strong thermodynamic driving force for precipitation and radiation-enhanced diffusion.[2] The formation mechanism of MNSPs, however, is not as clear. There are debates in the field regarding whether the MNSPs are irradiation-induced or irradiation-enhanced. Some argued that the MNSPs are not thermodynamically stable phases, but are solute clusters induced by non-equilibrium processes, such as radiation-induced segregation (RIS), during irradiation.[3,4] On the other hand, thermodynamic models predict stable MNSP phases at the reactor service temperature.[5]

One approach to answer the open question regarding the thermodynamic stability of MNSPs is to conduct post-irradiation annealing (PIA). If PIA leads to further coarsening of the MNSPs formed during irradiation, the MNSPs should be thermodynamically stable. The difficulty of such study, however, is that the kinetics is very sluggish at the reactor service temperature without radiation-enhanced diffusion. Consequently, PIA experiments need to be carried out at higher temperatures, at which the equilibrium volume fraction of the MNSPs can be small, even if the MNSPs are eventually thermodynamically stable. Recently, Wells et al. annealed neutron-irradiated steel samples at 400 and 425°C and characterization showed that small volume fraction of MNSPs were still present after 57 weeks at 400°C and 29 weeks at 425°C.[6] Thus, the experiments strongly support the argument that the MNSPs are indeed an irradiation-enhanced thermodynamically stable phase.

The new data from the PIA experiments provide valuable information that can be used for parameterization of recently-developed models for precipitation in RPV alloys. The PIA experimental data used in this report were collected by collaborators Dr. Peter Wells and Professor G. Robert Odette at the University of California, Santa Barbara. The PIA experimental data include atom probe measurements of particle size distribution and precipitate composition for alloys CM6 (nominal composition 1.50at.%Mn-1.57%Ni-0.33%Si) and LG (nominal composition 1.36at.%Mn-0.69%Ni-0.43%Si) annealed at 425°C for annealing times of 1, 7, 17, and 29 weeks and 400°C for annealing times of 29 and 57 weeks. This report introduces a newly-developed kinetic Monte Carlo (KMC) model, and compares the model prediction to the experimental PIA observations. In addition, this report provides updates on the recent efforts to refine the previously-developed cluster dynamics (CD) model.

2. METHODS

2.1 Kinetic Monte Carlo Simulations

2.1.1 Kinetic Monte Carlo Model

The KMC model is developed based on the framework of the model by Enrique and Bellon,[7] and directly modified from the code developed by Shu et al.,[8] adding multinary simulation capability and body-centered cubic (bcc) structural information.

A bcc rigid lattice is constructed from an N×N×N (N = 64 or 256) rhombohedral crystal with periodic boundary conditions. The faces of rhombohedron correspond to {110} planes of the bcc crystal. Atoms migrate by thermally-activated jumps, assisted by nearest-neighbor atom-vacancy exchanges. A single vacancy is introduced into the system. Nearest-neighbor atomic pair interactions (ε_{XY}) and atom-vacancy interactions (ε_{XV}) are used to model cohesion and vacancy formation energies of the system, and their fitting is detailed in Subsection 2.1.2. Homo-atomic pair interactions (i.e., interactions between atoms of the same chemistry) are related to cohesive energies through:

$$E_{coh}^{X} = \frac{Z}{2}\varepsilon_{XX} \tag{1}$$

where

Z = nearest-neighbor site coordination number (Z = 8 for bcc structure).

Hetero-atomic interactions (i.e., interactions between atoms with different chemistry) are defined through the ordering energy as:

$$\omega_{XY} = 2\varepsilon_{XY} - \varepsilon_{XX} - \varepsilon_{YY} \tag{2}$$

The value of ω_{XY} determines the shape of the binary *X*-*Y* phase diagram. Effective atom-defect pair interactions are used to reproduce the values of vacancy defect formation energies, defined as:

$$E_{XV}^{f} = Z\varepsilon_{XV} - \frac{Z}{2}\varepsilon_{XX}{}_{9} \tag{3}$$

The frequency of the thermal jumps is determined using standard rate theory. The attempt frequency is set to be a constant equal to $6\times10^{12}\,s^{-1}$, similar to the atomic vibration frequency. Activation energy is calculated using:

$$E_a^X = E_0^{mig} + E_a^{saddle} \tag{4}$$

where

E_a^{saddle} = saddle-point energy.

E_a^{saddle} is calculated using the final-initial-state energy approximation:

$$E_a^{saddle} = \frac{E_f - E_i}{2} \tag{5}$$

where

E_i = system total energies before the jump of the vacancy

E_f = system total energies after the jump of the vacancy.

The reference activation energy E_0^{mig} is assumed to be dependent on the chemical species of the migrating atom, and the value of E_0^{mig} is taken from Ref. 10.

During the simulation, time is incremented using a residence-time algorithm.[11] Since a single vacancy is introduced in the simulation cell, a fixed vacancy concentration is unphysically imposed. Thus, a rescaling of the KMC time t_{MC} is needed to obtain the physical time t that can be directly compared with the experiments. The rescaling follows the approach proposed by Nastar and Soisson.[12]:

$$t = t_{MC} \frac{C_V^{KMC}(X)}{C_V^{eq}(X)} \tag{6}$$

where

$C_V^{KMC}(X)$ = vacancy concentration in phase *X*, measured in the KMC simulation

$C_V^{eq}(X)$ = equilibrium vacancy concentration in *X* phase, calculated using the vacancy formation energy.

2.1.2 Kinetic Monte Carlo Model Parameterization

The homo-atomic pair interactions ε_{XX} for determining E_i and E_f are determined from measured cohesive energies for the bcc phase of the pure element. The hetero-atomic pair interactions ε_{XY} are obtained from molar excess free energies (G_{AB}^m), calculated by the CALPHAD method. Specifically, assuming a regular solution model, one can write:

$$G_{AB}^m = x_A G_0^A + x_B G_0^B + RTx_A \ln x_A + RTx_B \ln x_B + x_A x_B \Omega_{AB} \tag{7}$$

where

$$\Omega_{AB} = \frac{Z}{2} N_A \omega_{AB}$$

Ω_{AB} is available or can be fit from the CALPHAD model for G_{AB}^m and connects the CALPHAD output to the KMC input.

Ω_{Mn-Ni} is further adjusted so that the volume fraction obtained using the KMC simulation is the same as the CALPHAD prediction using the CM6 alloy nominal composition, after considering the Gibbs-Thomson effect, shown in Figure 1(a). The LG alloy composition is used to validate the quality of the parameterization. Comparison of the KMC and CALPHAD calculation is plotted in Figure 1(b), showing good agreement.

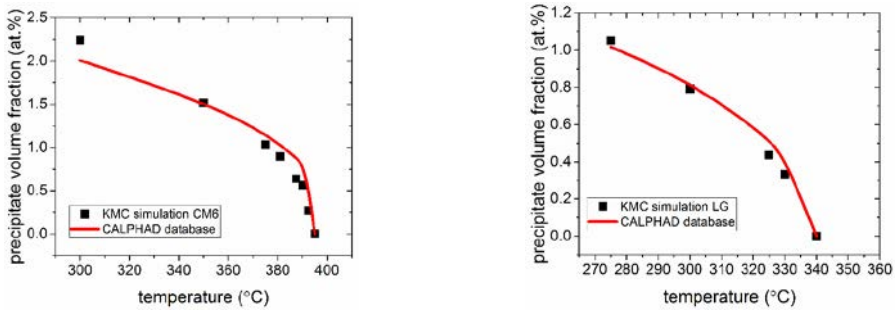

(a) (b)

Figure 1. Volume fraction of Mn-Ni-Si precipitates measured in kinetic Monte Carlo simulations and calculated using CALPHAD. (a) CM6 nominal composition; (b) LG nominal composition.

Finally, Ω_{Mn-Ni} is slightly adjusted again to fit the atom probe data obtained from PIA of the CM6 alloy at 425°C, using the volume fraction and Si concentration at a long annealing time. Ω_{Ni-Si} is also fitted with the atom probe data, using the time evolution of Si composition in the precipitates.[6] These changes do not alter the precipitate volume fraction–temperature curve (as plotted in Figure 1) significantly.

Table 1 lists the chosen parameter set.

Table 1. Interaction parameters used in simulation.

Ω_{AB} (eV)	Mn	Ni	Si
Fe	0.094	0.007	−1.542
Mn	—	−0.465	−0.907
Ni	—	—	−1.850

E_{coh}^{X} (eV)	Fe	Mn	Ni	Si
	−4.28	−2.92	−4.34	−4.03

2.2 Cluster Dynamics Simulations

As described in previous milestones, the CD method gives the size distribution of clusters by solving a series of ordinary differential equations as follows:

$$\frac{\partial f(n,t)}{\partial t} = w_{n-1,n}^{(+)}\{f(n-1,t) - f(n,t)\exp[\frac{\Delta G(n) - \Delta G(n-1)}{k_B T}]\}$$
$$+w_{n,n+1}^{(+)}\{-f(n,t) + f(n+1,t)\exp[\frac{\Delta G(n+1) - \Delta G(n)}{k_B T}]\} \quad (8)$$

where

$f(n,t)$ = concentration of clusters containing *n* atoms at time *t*.

The coefficient $w_{n,n+1}^{(+)}$ s are the rates at which clusters of size *n* absorb single atoms to grow to size *n+1*, and $\Delta G(n)$ is the formation energy of clusters with *n* atoms. More details regarding this method can be found in Ref. 13, 14, 15, and 16.

For a system containing *k* precipitating components, these rates are given by:

$$w_{n,n+1}^{(+)} = \left[\sum_{i=1}^{k}\left(\frac{\nu_{i\alpha}^2}{w_{n_i,n_i+1}^{(+)}}\right)\right]^{-1} \quad (9)$$

where

$w_{n_i,n_i+1}^{(+)}$ = rate at which clusters of size *n* gain one atom of species *i*.

The parameter $v_{i\alpha}$ accounts for the change in the composition of component *i* as the cluster grows from size *n* to *n+1*. It is defined by the following expression:

$$v_{i\alpha} = x_{i\alpha} + n\frac{dx_{i\alpha}}{dn} \tag{10}$$

where

$x_{i\alpha}$ = atomic fraction of component *i* in clusters of size *n*.

Here it is assumed that $x_{i\alpha}$ does not change with *n*, thus $v_{i\alpha}$ equals $x_{i\alpha}$.

For diffusion-limited growth of the clusters, the absorption rate becomes:

$$\omega_{n,n+1}^{(+)} = 4\pi c_\beta a_\alpha D_{eff}^d n^{1/3} \tag{11}$$

$$\frac{1}{D_{eff}^d} = \sum_{i=1}^{k} \frac{v_{i\alpha}^2}{x_{i\beta} D_i} \tag{12}$$

where

C_β = total volume concentration of the particles of the different components in the ambient phase

$x_{i\beta}$ = molar fraction of the different components in the ambient phase.

The emission rate is given by:

$$\omega_{n+1,n}^{(-)} = \omega_{n,n+1}^{(+)} \exp\left(\frac{\Delta G(n+1) - \Delta G(n)}{k_B T}\right) \tag{13}$$

where

$\Delta G(n)$ = formation energy of clusters with *n* atoms from the matrix, which can be written as:

$$\Delta G(n) = n\left(g_p - \sum_i x_i \mu_i\right) + \sigma(n) \tag{14}$$

where

g_p = free energy per atom of the precipitate phase

μ_i = chemical potential of component I in the matrix

$\sigma(n)$ = interfacial energy of a cluster of size *n*.

With this form, the difference $\Delta G(n+1)-\Delta G(n)$ reduces to:

$$\Delta G(n+1) - \Delta G(n) = g_p - \sum_i x_i \mu_i + [\sigma(n+1) - \sigma(n)] \tag{15}$$

In dilute alloys, the chemical potentials can be written as:

$$\mu_i = \mu_i^0 + kT[\ln\gamma_i + \ln c_i] \tag{16}$$

When the matrix phase is in equilibrium with the precipitate phase, it can be written as:

$$\begin{aligned} g_p - \sum_i x_i \mu_i &= 0 \\ g_p - \sum_i x_i[\mu_i^0 + kT\ln\gamma_i] &= kT\sum_i x_i \ln c_i \end{aligned} \tag{17}$$

In dilute alloys, the emission rate can be written as:

$$\omega_{n+1,n}^{(-)} = \omega_{n,n+1}^{(+)} \frac{\overline{\prod_i} c_i^{x_i}}{\prod_i c_i^{x_i}} \exp\left(\frac{\sigma(n+1) - \sigma(n)}{k_B T}\right) \quad (18)$$

The over bar on the solute product indicates the value of the solute product in equilibrium.

The distribution function f(n=1,t) at n=1 is described as:

$$f(n=1,t) = c_\beta \prod_{i=1}^{k} x_{i\beta}^{x_{i\alpha}} \quad (19)$$

3. RESULTS

3.1 Kinetic Monte Carlo Simulation of Isothermal Annealing of CM6 Steels

CM6 steel is a Cu-free, high-Ni steel. In the simulation, since the primary interest is in the evolution MNSPs, the elements other than Fe, Mn, Ni, and Si are not included. In addition, to compare our simulations to the experiments in a consistent way, the composition measured in the as-irradiated atom probe tips is used instead of the nominal composition of the steel. When plotting the simulation results and experimental measurement together, the experimental results obtained from a tip whose composition is similar to the as-irradiated tip were chosen. Table 2 lists the tip compositions used in the simulation. Note that the tip composition of Ni is higher than the nominal composition, while that of Mn is lower than the nominal composition. This difference may be at least partially attributed to the formation of carbides, which are rich in Mn.[17]

Table 2. Nominal composition of CM6 steel and as-irradiated tip composition used in simulation.

Composition	Cu	Ni	Mn	Mo	P	C	Si	Fe
Nominal composition	0.02	1.57	1.50	0.31	0.012	0.68	0.33	bal.
Composition in simulation	0	1.69	1.42	0	0	0	0.39	bal.

To simulate the PIA, at the beginning of the simulation, pre-existing precipitates were randomly put into the simulation cell. The initial composition of the precipitates, precipitate size distribution, and number density was directly taken from the atom probe results. After generating the precipitates, the initial configuration yields similar volume fraction as in the experiments.

We first consider the isothermal annealing of CM6 steel at 425°C. Figure 2 shows a series of microstructures at different annealing times in a typical simulation run. Clearly, as annealing time increases, there are fewer and fewer MNSPs in the simulation cell: smaller precipitates dissolve, while the larger precipitates grow. To compare the simulation and experiments quantitatively, Figure 3 shows the average precipitate diameter, number density, and volume fraction as a function of annealing time, predicted by the KMC simulation, as well as measured from atom probe tomography (APT) experiments. The simulation reproduces all the significant trends observed in the experiments. Upon annealing, the average precipitate diameter <d> first decreases, due to the higher Mn, Ni, and Si solubility at 425°C than at 290°C (reactor service temperature at which the irradiation was carried out). As annealing continues, after the end of the initial stage of MNSP dissolution, normal Ostwald ripening occurs, leading to increasing average precipitate diameter. This understanding is supported by the fact that after 10 weeks, while the average precipitate size increases and the MNSP number density decreases, the volume fraction increases only slightly over time. Overall, the predictions made by the KMC simulation and experimental results agree well, supporting the validity of the KMC model for this type of simulation.

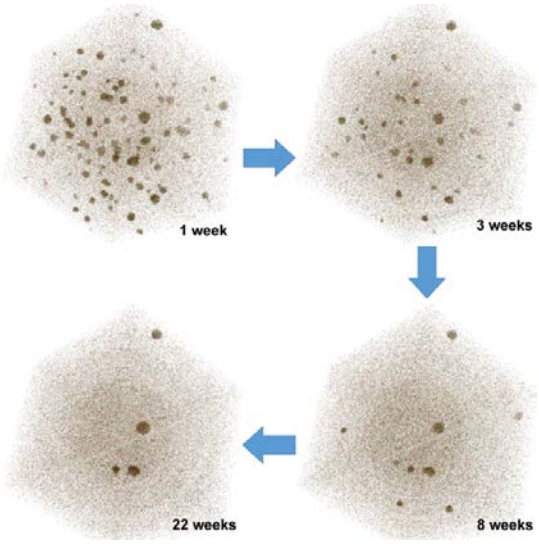

Figure 2. Typical sequence of microstructure evolution during post-irradiation annealing of CM6 steel.

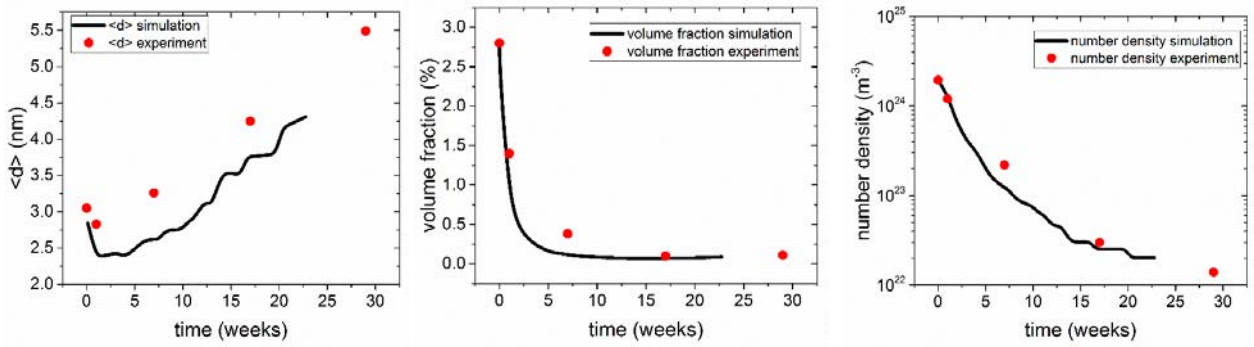

Figure 3. Average precipitate diameter <d>, precipitate number density, and precipitate volume fraction as function of annealing time, from both kinetic Monte Carlo simulations (black lines) and atom probe tomography experiments (red dots), for annealing at 425°C.

To further validate the parameterization, Figure 4 shows the results of isothermal annealing of CM6 steel at 400°C. Similar to the 425°Cannealing, the experiments show reasonably good agreement.

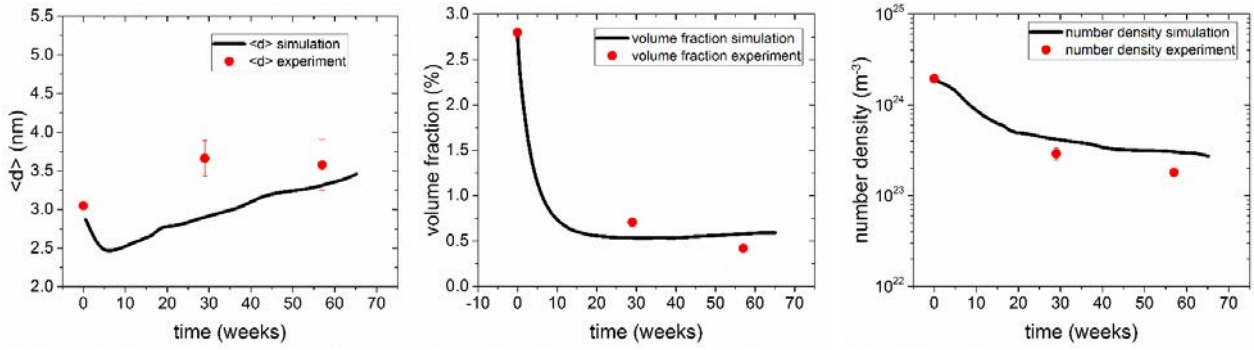

Figure 4. Average precipitate diameter <d>, precipitate number density, and precipitate volume fraction as function of annealing time, from both kinetic Monte Carlo simulations (black lines) and atom probe tomography experiments (red dots), for annealing at 400°C.

To study how the precipitates grow, Figure 5 plots the time evolution of the molar fraction of Mn, Ni, and Si atoms in the precipitate, both from the simulations and experiments, for the 425°C annealing. The simulation shows qualitative agreement with the experiments. Most importantly, the simulation captures the fact that as the precipitate grows, the Ni molar fraction does not change significantly, and that the Mn fraction increases while the Si fraction decreases. This suggests that during growth of the precipitates, Si atoms join to the MNSPs at a slower rate than the other two elements, indicating that the equilibrium molar fraction of Si is lower than that of the precipitates in the as-irradiated sample.

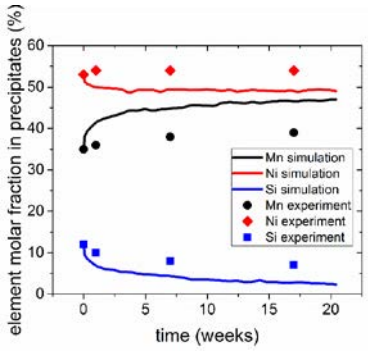

Figure 5. Time evolution of molar fraction of Mn, Ni, and Si in precipitate, from both simulations and experiments.

To investigate the details of the decreasing Si molar fraction during annealing, specifically to see whether this decrease is uniform within the precipitate, Figure 6 shows the Si molar fraction measured in concentric spherical shells as a function of the distance to the precipitate center of mass. Figure 6(a) shows that in the simulations, from the precipitate core to the precipitate/matrix interface, the Si molar fraction decreases, forming a Si-depleted shell. Further into the matrix, the Si molar fraction increases and plateaus at the bulk value. Thus, through the whole plot, the data make a V-shaped profile. In Figure 6(b), the same profiles are plotted using the APT data, for the as-irradiated sample, as well as the annealed samples, from 1 to 17 weeks. The first observation is that, at larger distances from the core, the Si molar fraction of the three annealed samples all reach the same bulk value, ~10%. However, for the as-irradiated sample, this bulk value is smaller, indicating that for the as-irradiated sample, the precipitates are richer in Si. In addition, for all the annealed samples, the profiles all show the V shape, consistent with the prediction of the KMC simulations. However, the Si molar fraction of the as-irradiated sample does not show the V shape, but a monotonic decrease, until it reaches the bulk value. *This observation suggests that during the irradiation, when the MNSPs form, Si atoms are driven into the precipitates, possibly by RIS, to a concentration higher than the equilibrium value.* This result provides a new understanding that Si RIS may play an important role in the evolution of the MNSPs.

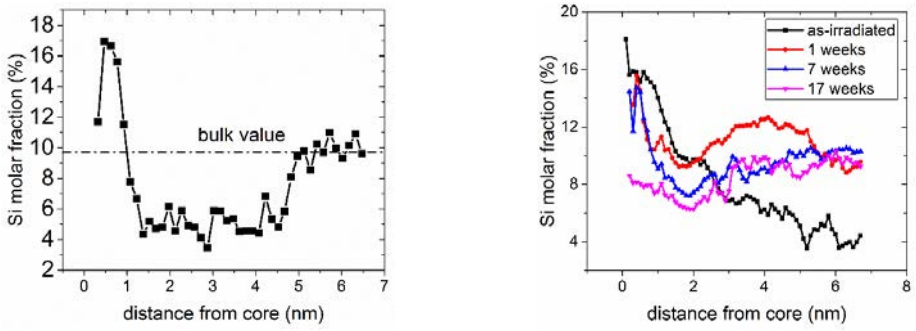

(a) (b)

Figure 6. Si molar fraction measured in concentric shells, as function of distance from precipitate core (center of mass of precipitate). (a) Simulated CM6 alloy annealed for 17 weeks at 425°C; (b) atom probe

tomography results for CM6 steels in as-irradiated condition, as well as annealed for different times at 425°C.

3.2 Cluster Dynamics

3.2.1 Comparison of Model to Isothermal Annealing of CM6 Steels

This subsection explores comparison of our CD model with the PIA data to better assess and refine the model, similarly to the studies described in Subsection 3.1 for the KMC model. We compare to annealing experiments carried out for the CM6 steels (nominal composition listed in Table 2). According to results from the TCAL2 database[18] from the Thermo-Calc company, only the T6 phase ($Mn(Ni,Si)_2$) will form around this composition. Thus, the T6 phase is the only phase that is modeled in the CD model. Table 3 and Table 4 list all the parameters needed. Equilibrium solute products are calculated from the TCAL2 database,[18] interfacial energy is from the CD model fitted to the irradiation data for the MNSPs,[19] and the diffusion coefficients are obtained from the literature.[20,21,22]

Table 3. Thermodynamic parameters for cluster dynamics model.

Parameter	Value	Ref.
Equilibrium solute product at 425°C	7.95×10^{-3}	18
Equilibrium solute product at 400°C	6.57×10^{-3}	18
Interfacial energy (mJ/m^2)	170	19

Table 4. Diffusion coefficients in cluster dynamics model.

Element	Q (kJ/mol)	D_0 (cm^2/s)	Ref.
Mn	251.626	0.78	20
Ni	245.765	1.40	21
Si	220.496	0.78	22

At 425°C, atom probe tips were taken from samples annealed for 1, 7, 17, and 29 weeks. Table 5 lists the corresponding average tip compositions and experimental data. Figure 7 shows the comparison between simulation results and experimental data at 425°C. Qualitatively, the simulation shows the dissolving and then coarsening of precipitates, and follows the same trend as experiments that as time progresses number density increases, mean radius increases, and volume fraction decreases (very fast at the beginning then more slowly). However, quantitatively the calculation result gives higher number density and volume fraction, and much lower mean radius compared to experimental data.

Table 5. Experimental data at 425°C.

Time (weeks)	Alloy Composition (at.%)			Experimental Results		
	Mn	Ni	Si	Number Density ($10^{23}/m^3$)	Mean Radius (nm)	Volume Fraction (%)
As irradiated	1.42	1.69	0.39	19	1.53	2.81
1	1.17	1.43	0.35	12	1.42	1.46
7	1.38	1.64	0.36	2.2	1.63	0.38
17	1.38	1.63	0.34	0.3	2.13	0.10
29	1.29	1.56	0.36	0.14	2.75	0.11

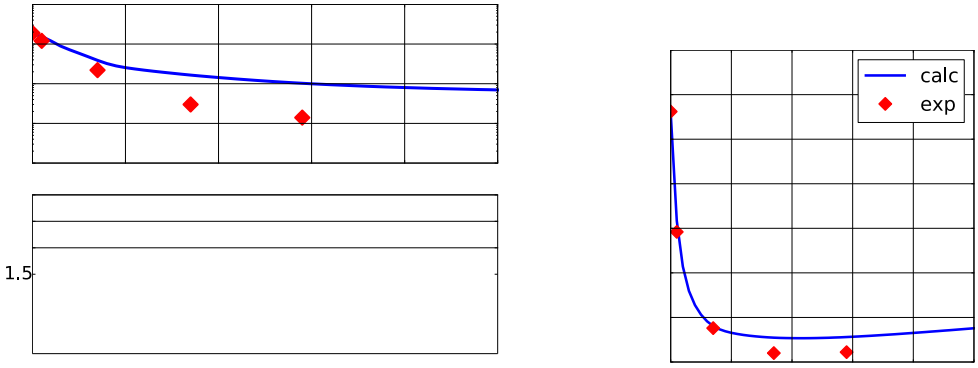

Figure 7. Comparison between calculation results and experimental data at 425°C.

Figure 8 shows the comparison of size distribution of precipitates between experimental data and simulation results at 7 and 17 weeks. Figure 7 and Figure 8 together show that simulation results give higher number density for small clusters (<1.0 nm) and lower number density for large clusters (>2.5 nm) compared to experiments.

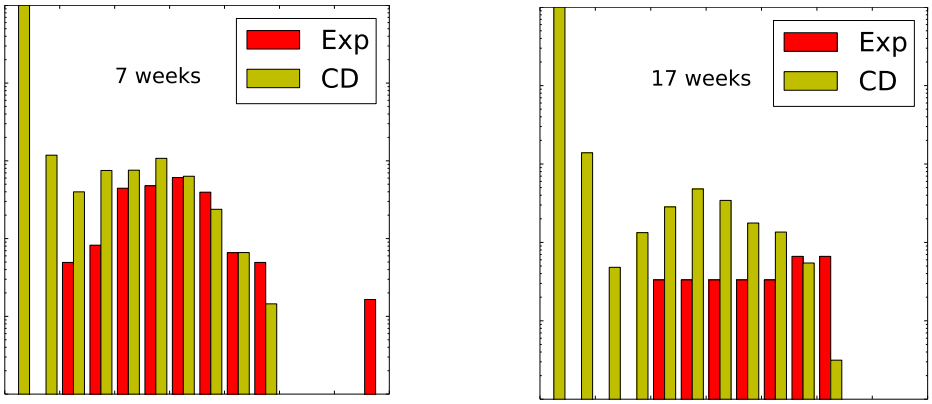

(a) (b)

Figure 8. Comparison of size distribution between cluster dynamics model and experimental data at 425°C. (a) 1 week; (b) 17 weeks.

At 400°C, experiments were done at 29 and 57 weeks. Table 6 lists the experimental data. Simulations were conducted with measured tip compositions and Figure 9 shows the results. Similar to the above comparisons at 425°C, Figure 9 shows that simulation results give higher number density, lower mean radius, and higher volume fraction compared to the experimental data. However, the discrepancies are somewhat smaller.

Table 6. Experimental data at 400°C.

Time (weeks)	APT Run No.	Alloy Composition (at.%)			Experimental Results		
		Mn	Ni	Si	Number Density ($10^{23}/m^3$)	Mean Radius (nm)	Volume Fraction (%)
29	4298	1.41	1.67	0.39	2.91	1.83	0.71
57	5094	1.36	1.67	0.41	0.18	1.79	0.42

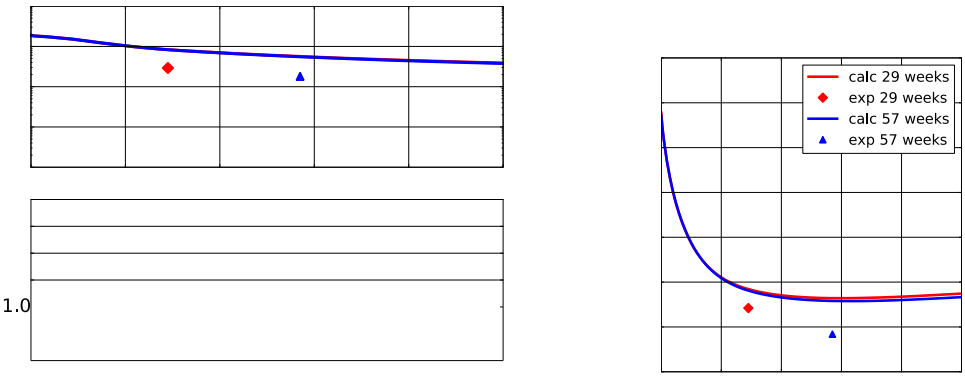

Figure 9. Comparison between calculation results and experimental data at 400°C.

The nature and scale of the deviations between simulation and calculation results shown for comparisons to PIA generally suggest good qualitative agreement and qualitative predictive ability for the model, but that there are at least small errors in the thermodynamics being used in the simulations. More specifically, the combined results suggest that the simulations are overstabilizing the smaller particles, which should be dissolving faster, and, correspondingly not growing the larger particles as much as seen in the experiment. In addition, the overall volume fraction is somewhat too high during the evolution, but this may also be a result of the incorrect dissolution of the smaller particles.

The discrepancies may have several causes, of which most likely are:

1. Errors in the CALPHAD thermodynamic model
2. Cluster composition evolution occurs in ways that are not presently captured by the CD model
3. Interfacial energy of precipitates should be size dependent.

Cause 1 is likely to occur to some extent as the CALPHAD thermodynamic database is generally fitted to higher temperature data than the temperature range in which we are applying it towards.

Cause 2 is as likely as significant as cause 1, as composition changes are clearly occurring during annealing, as was shown in the KMC simulations and atom probe data discussed in Subsection 3.1. In particular, there is no RIS included in the CD model and the particle composition is fixed during the particle evolution to stoichiometric phases. The missing compositional changes will almost certainly have some impact on stability and interfacial energies, which in turn will alter the precipitate size, number density, and volume fraction values.

Finally, Cause 3 is likely to occur, as changing interfacial energy is a known effect in very small nanoparticles. Specifically, very small particles have increasing numbers of high energy edge and corner atoms, leading to an increasing interfacial energy at very small sizes (~1 nm) versus larger sizes (~10 nm).

There are many other possible sources of discrepancies between the CD model and annealing experiments, ranging from the possibility that the detection limit of atom probe and those assumed in our simulations (only clusters above 65 atoms are treated as detectable) are not identical to errors introduced by the mean field approximations in CD. However, at this point, based on our simulations, Causes 1, 2, and 3 are the most likely causes of the discrepancies and they have been the focus of ongoing work. Subsection 3.2.2 discusses an initial effort to explore the effects of thermodynamic errors and RIS. We plan to continue with these efforts and explore the addition of size dependence of interfacial energy in future work.

3.2.2 Improving Cluster Dynamics Model—Refining Thermodynamics and Including Radiation-Induced Segregation

As mentioned in Subsections 3.1 and 3.2.1, there is increasing evidence from the annealing studies that CALPHAD model errors and/or RIS are likely to be playing a role in the MNSP evolution. This subsection explores an initial effort to consider both possible effects in the CD model.

As additional understanding of how thermodynamic errors and RIS effects might be playing a role in the MNSP evolution, we reconsider our previous modeling of very high fluence irradiation steels. In previous calculations,[5] the equilibrium volume fraction of RPV steels was calculated with two databases and agreed well with very high fluence ($1.1\times10^{25}m^{-2}$) experimental data measured by APT, which is considered to give an equilibrium volume fraction. Figure 10 shows the comparison. However, as the precipitates are around 1 to 2 nm in radius, the Gibbs-Thomson effect should also be considered when doing the calculations. Figure 11 shows the Gibbs-Thomson effect on the final solute fraction by calculating the equilibrium volume fraction of precipitates in six alloys[5,17] with our in-house UW1 database, considering a series of different precipitate radius from 0.5 to 2 nm and assuming interfacial energies as the best-fit results from our previous CD model.[19] This analysis shows that after considering the Gibbs-Thomson effect, the calculation results will be lower than experimental data, especially for low-solute alloys. Two likely explanations for these discrepancies are errors in the thermodynamic database or RIS effects. Given the evidence for RIS from Subsections 3.1 and 3.2.1, it is most likely that these discrepancies are at least in part a RIS effect. However, we explore extending the model in the following subsections to address both correcting thermodynamic errors and including RIS effects.

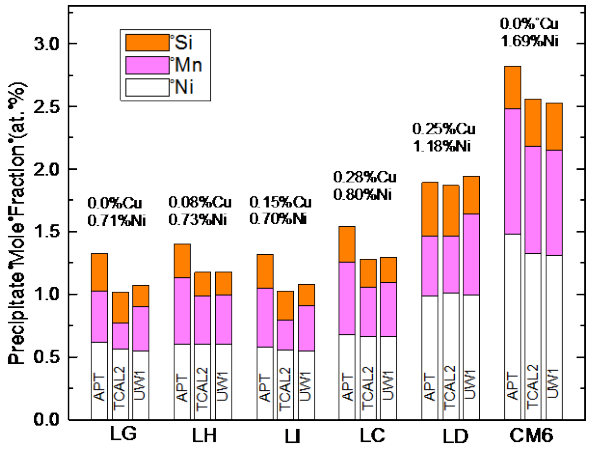

Figure 10. Equilibrium precipitate mole fraction calculated from CALPHAD databases and compared to experimental data.

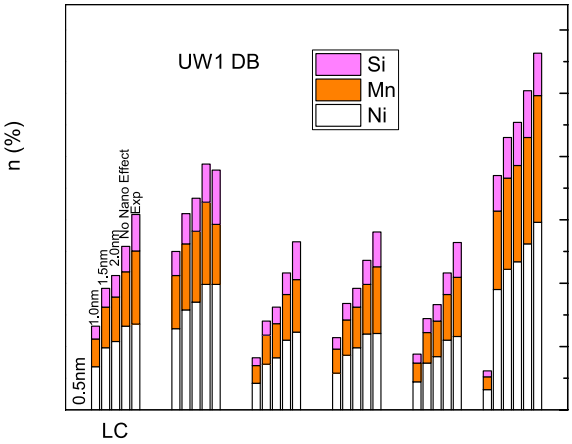

Figure 11. Gibbs-Thomson effect on solute fraction of precipitates, where radii for each precipitate are noted. Data from UW1 in-house database.

3.2.2.1 Revising CALPHAD Thermodynamics Model. This subsection describes our effort to refit the CALPHAD thermodynamics to match the correct volume fractions in Figure 8. The CALPHAD thermodynamics for the phases in our CD model are determined by the solubility product (see Subsection 2.2), which is a single parameter for each phase at a given temperature. However, given the fact that the final equilibrium volume fraction of nano-size precipitates will be determined from both the solubility product and interfacial energies of precipitates, the thermodynamics of MNSPs are revised in two steps. First, for each set of interfacial energies, an optimal set of solubility product will be obtained by matching the volume fraction of precipitates to the very high fluence experimental data in Figure 8.[17] Second, these different sets of interfacial energies and solubility products will be put into the CD model together with two other fitting parameters (heterogeneous nucleation size and heterogeneous nucleation rate coefficient) to obtain the number density and mean radius of precipitates and compare to all experimental data irradiated under different flux and measured at different fluence. In this way, we can obtain a revised thermodynamic model consistent with the high fluence data and assess the new thermodynamics against the entire database of irradiated samples.

Figure 12 shows the root mean square difference (RMSD) of volume fraction between calculation and experimental data by modifying formation energy of two precipitate phases, which is calculated by:

$$RMSD(V) = \sqrt{\frac{\sum_{i=1}^{N}(V_i^{calc}/V_i^{exp} - V_i^{exp}/V_i^{exp})}{N}} \quad (20)$$

where

V_i^{calc} = calculation result of volume fraction of *i*th alloy

V_i^{exp} = experimental measured volume fraction of *i*th alloy

N = total number of alloys considered. Here N is 6.

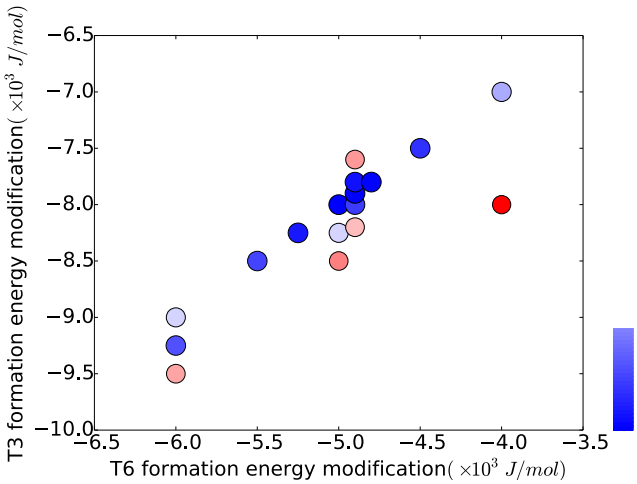

Figure 12. Root mean square difference of volume fraction between calculation and experimental data by modifying formation energy of two precipitate phases.

Figure 12 shows that a modification of −4900J/mol for the T6 phase and −7900J/mol for the T3 phase gives the best fit to experimental data, yielding, and RMS error versus experiment of 6.41% of the experimental data.

Figure 13 shows the comparison of precipitate solute fraction to experimental data before (without Gibbs-Thomson effect) and after (including Gibbs-Thomson effect) thermo-modification, which shows that after thermo-modification calculation results are somewhat closer to the experimental data. Furthermore, when comparing the models where the full Gibbs-Thomson effect is included, the results of our new model are much more accurate compared to the experiment, as would be expected after such a fitting procedure.

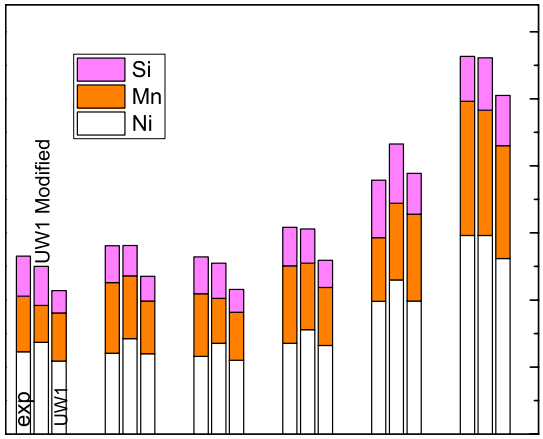

Figure 13. Comparison between experimental data and calculation results before and after thermo-modification.

With the modified thermodynamics, all fitting parameters in the CD model are refit to experimental data.[17,19] Table 7 lists the ranges of values chosen for fitting the model, where five values are chosen for each parameter and cover a wide range of reasonable values.

Table 7. Fitting parameters of cluster dynamics model.

Parameter	1	2	3	4	5
Two interfacial energies (mJ/m^2)	250	300	350	400	450
Heterogeneous nucleation size	20	30	40	50	60
Heterogeneous nucleation rate (cluster/cascade)	0.01	0.03	0.05	0.07	0.09

By gridding the four-dimensional parameter space with these five values, 625 separate possible models are sampled and the best ones chosen. The RMSD for number density, mean radius, and volume fraction is calculated to obtain the best-fit parameters. Here the method for calculating mean radius and volume fraction are the same as in *Equation (20)*. The RMSD for number density is calculated using the following equation:

$$RMS(logN) = \sqrt{\frac{\sum_{i=1}^{n}(\log(N_i^{Calc}) - \log(N_i^{Exp}))^2}{n}} \quad (21)$$

RMSD(N) will be $10^{RMS(logN)}$. Table 8 lists the lowest RMSD for each separately of number density, mean radius, and volume fraction and the corresponding parameter values. Table 8 shows that best-fit result for different properties are at different ends of the values of the fitting parameters chosen, which means a good fit cannot be obtained for these three properties with the same set of parameters.

Table 8. Best-fit parameter set for different properties (number density, mean radius, and volume fraction).

Parameter		Number Density	Mean Radius	Volume Fraction
Lowest RMSD value		1.30	16.8%	100%
Values for fitting parameters	Heterogeneous nucleation size	20	60	20
	Heterogeneous nucleation rate (cluster/cascade)	0.05	0.09	0.01
	T3 interfacial energy (mJ/m^2)	450	450	450
	T6 interfacial energy (mJ/m^2)	450	250	450

After considering all three properties, a combined RMSD is calculated by:

$$RMSD^{Combine} = \frac{RMSD(N)}{3} + \frac{RMSD(R)}{30\%} + \frac{RMSD(V)}{10\%} \quad (22)$$

The best fit will occur with heterogeneous nucleation size 20 atoms, heterogeneous nucleation rate 0.01 cluster/cascade, and interfacial energies for both phases 450 mJ/m^2. The RMSD values for number density, mean radius, and volume fraction with this set of parameters are 2.43, 63.2%, and 100%, respectively.

Figure 14 shows the comparison between calculation and experimental data with best-fit parameters. It gives higher number density and lower mean radius compared to experimental data. And, as stated above, it is not possible to match experimental data simultaneously for number density, mean radius, and volume fraction.

Figure 14. Comparison between calculation and experimental data with best-fit parameters.

While the failure to achieve a robust model by modifying the thermodynamics is in some ways disappointing. it actually provides very useful information. In particular, these results strongly suggest that errors in the CALPHAD thermodynamics are not the main reason that cause disagreement between calculation results and experimental data for very-high-flux and very-high-fluence data. We note that it is the availability of literally dozens of high-quality measurements from the University of California, Santa Barbara, group that enable this kind of powerful testing and winnowing down of model hypotheses.

3.2.2.2 Radiation-Induced Segregation Effects. As discussed in Subsection 3.2.2, another possible cause for the difference between calculation results and both the annealing and very high fluence experimental data is RIS. To explore the possible effect of RIS on the evolution of MNSPs, a one-dimensional RIS calculation is effectively included within the CD model.

Several quite severe assumptions and approximations are made in this mode as follows:

1. The interface between precipitates and matrix are perfect sinks into which vacancy and interstitials will be absorbed once they arrive at the interface.
2. The RIS profile as a function of distance to sinks is proportional to the initial composition of the matrix.
3. The one-dimensional RIS profile to perfect sinks is applied to the radial direction from the precipitates.
4. The RIS profile over the first 1 nm near the precipitate can be averaged to provide the effective composition near precipitate interface.
5. The RIS profile measured building up at a grain boundary can be transferred to the precipitate interface to predict local composition changes at the interface and associated changes in local chemical potential.

Figure 15 shows a schematic plot of the RIS profile applied to a precipitate.

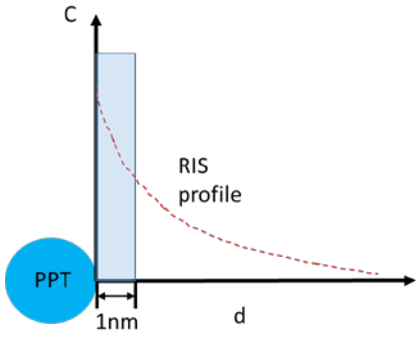

Figure 15. Schematic plot showing radiation-induced segregation effect in cluster dynamics model.

Both Si and Ni RIS effect are considered in the model. Parameters are fitted from experimental data of RIS effect on grain boundaries in T91 alloys under irradiation.[23] Two Cu-free steels, CM6 (Fe-1.42at.%Mn-1.69%Ni-0.39%Si) and LG (Fe-0.87at.%Mn-0.73%Ni-0.43%Si), are studied first to test the effect of RIS. The experiments we use for validation irradiated these alloys at a very high flux of $2.3\times10^{23}m^{-2}s^{-1}$ and to a very high fluence of $1.1\times10^{25}m^{-2}$. Please note that no further fitting has been done specifically for RPV steels. Figure 16 shows the results after adding RIS effect. After adding RIS effect, especially for low-solute alloy LG, much more precipitate has formed, which agrees well with experimental data for number density, mean radius, and volume fraction. These results indicate that RIS is potentially the source of the previous lower-calculated volume fraction compared to experimental data shown in Figure 11.

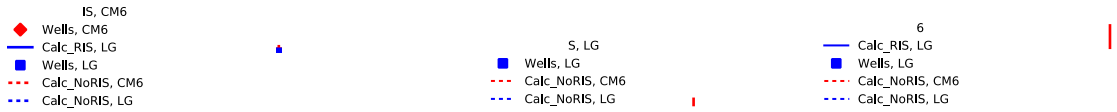

Figure 16. Comparison between calculation and experimental for low-Cu alloys before and after adding radiation-induced segregation effect.

After these encouraging initial studies, the RIS effect was introduced into our CD models for other low-Cu systems[17,19,24,25] and parameters were refitted for the CD model. Two sets of parameter fittings have been done, first with a relative coarse grid and then with a finer grid for the parameters. Table 9 lists the first set of fitting parameters. The RMSD for number density, mean radius, and volume fraction are calculated to obtain the best-fit parameters, which are found with interfacial energy of T3 at 220 mJ/m^2, interfacial energy of T6 at 240 mJ/m^2, heterogeneous nucleation size at 40 atoms, and heterogeneous nucleation rate coefficient at 0.12 cluster/cascade. The second set of parameter fittings was done with a finer grid around this best-fit parameter set. Table 10 lists the parameters chosen for this set. Table 11 lists the final best-fit parameters.

Table 9. First set of fitting parameters after adding radiation-induced segregation effect.

Parameter	1	2	3	4
Two interfacial energies (mJ/m^2)	180	200	220	240
Heterogeneous nucleation size	30	40	50	—
Heterogeneous nucleation rate coefficient (cluster/cascade)	0.03	0.06	0.09	0.12

Table 10. Second set of fitting parameters after adding radiation-induced segregation effect.

Parameter	1	2	3	4	5
T3 interfacial energy (mJ/m^2)	200	210	220	230	240
T6 interfacial energy (mJ/m^2)	220	230	240	250	260
Heterogeneous nucleation rate (cluster/cascade)	0.10	0.11	0.12	0.13	0.14

Table 11. Best-fit parameters after adding radiation-induced segregation.

Parameter	Value
Interfacial energy of T3	220
Interfacial energy of T6	250
Heterogeneous nucleation size	40
Heterogeneous nucleation generation rate coefficient	0.14

Figure 17 shows the comparison between calculation results and experimental data after adding the RIS effect into the model and refitting the model parameters. Results are shown for all low-Cu RPV steels in our dataset. The RMSD between calculation results and experimental data are 1.41, 23.69%, and 126% for number density, mean radius, and volume fraction, respectively. Given that the root mean square statistics between calculation results and experimental data before adding the RIS effects were 1.47, 26.00%, and 62% for number density, mean radius, and volume fraction, respectively, no obvious improvements are obtained for the model when considering all systems including both low- and high-flux irradiation conditions.

Figure 17. Comparison between calculation results and experimental data after adding radiation-induced segregation.

In summary, while RIS effects are a likely cause for some of the disagreement between calculation results and high-flux very-high-fluence experimental data (see Figure 11), a full comparison to our total data set does not show any significant improvement associated with adding RIS effects to the model. However, the simple RIS model implemented here may not be accurate enough to explain data for all the wide range of flux and composition in our database, even if it does seem to help with certain alloys. Therefore, at this stage, we are not implementing the present RIS effects in the CD model but are exploring if a more accurate RIS model can be developed for use in the CD model.

4. SUMMARY

With the newly-available PIA data at both 425 and 400°C, we are able to refine both our KMC and CD models. Major results are as follows:

Kinetic Monte Carlo

- Good agreement is achieved between simulations and experiments on average size, number density, and volume fraction of precipitates at 425°C. The parameters can therefore be used in future studies considering irradiation effects.
- Simulations predict that during annealing, a Si-depleted shell near the MNSP/matrix interface forms, leading to decreasing molar fraction of Si in the MNSP. This prediction is consistent with the atom probe data.
- KMC and atom probe observations suggest that Si concentration in the MNSPs formed in irradiation condition is possibly increased by RIS when compared to what is expected at thermodynamic equilibrium.

Cluster Dynamics

- CD model gives qualitatively same trend as experimental annealing data, which is that precipitates quickly dissolve at the very beginning and then start to coarsen slowly.
- Quantitative comparison shows that the CD model gives higher number density, lower mean radius, and slightly higher volume fraction compared to experimental annealing data.
- Discrepancies with annealing and very-high-flux very-high-fluence irradiation experimental data suggest errors in the CALPHAD thermodynamics, incorrect CD modeling of precipitate and near precipitate composition (in particular, RIS effects), or lack of size-dependent surface energies may be leading to errors in the model.
- Exploration of possible changes in the CALPHAD thermodynamics (solute products) suggest that errors in the CALPHAD thermodynamics are not the main source of the errors between the experiments and CD model.
- Adding RIS effects into the CD model did improve the agreement with very-high-flux very-high-fluence experimental data but did not improve overall agreement with the experimental data. This suggests RIS effects are playing a role but that a more accurate model is needed to include this effect in the evolution of precipitates under all relevant experimental conditions.

These results suggest that future work should focus on developing an improved RIS model and including a size-dependent interfacial energy. Future modeling will also focus on integrating Cu to provide an integrate Cu-MNSP model.

5. REFERENCES

1. Odette, G.R., and R.K. Nanstad, 2009, Predictive reactor pressure vessel steel irradiation embrittlement models: Issues and opportunities, *JOM*, Vol. 61, pp. 17-23.
2. Odette, G.R., T. Yamamoto, and D. Klingensmith, 2005, On the effect of dose rate on irradiation hardening of RPV steels, *Philosophical Magazine*, Vol. 85, pp. 779-797.
3. Ngayam-Happy, R., C.S. Becquart, C. Domain, and L. Malerba, 2012, Formation and evolution of MnNi clusters in neutron irradiated dilute Fe alloys modelled by a first principle-based AKMC method, *Journal of Nuclear Materials*, Vol. 426, pp. 198-207.
4. Ngayam-Happy, R. C.S. Becquart, and C. Domain, 2013, First principle-based AKMC modelling of the formation and medium-term evolution of point defect and solute-rich clusters in a neutron irradiated complex Fe-CuMnNiSiP alloy representative of reactor pressure vessel steels, *Journal of Nuclear Materials*, Vol. 440, pp. 143-152.
5. Xiong, W., H. Ke, R. Krishnamurthy, P. Wells, L. Barnard, G.R. Odette, and D. Morgan, 2014, Thermodynamic models of low-temperature Mn-Ni-Si precipitation in reactor pressure vessel steels, *MRS Communications*, Vol. 4, pp. 101-105.
6. Wells, P., H.B. Ke, N. Almirall, D. Morgan, T. Yamamoto, and G.R. Odette, On the Thermal Stability of Features Formed in Highly Irradiated Reactor Pressure Vessel Steels.
7. Enrique, R.A., and P. Bellon, 2001, Compositional patterning in immiscible alloys driven by irradiation, *Phys. Rev. B*, Vol. 63, 134111.
8. Shu, S., P. Bellon, and R.S. Averback, 2015, Role of point-defect sinks on irradiation-induced compositional patterning in model binary alloys, *Phys. Rev. B*, Vol. 91, 214107.
9. Doyama, M., and J.S. Koehler, 1976, The relation between the formation energy of a vacancy and the nearest neighbor interactions in pure metals and liquid metals, *Acta Metallurgica*, Vol. 24, pp. 871-879.
10. Messina, L., M. Nastar, T. Garnier, C. Domain, and P. Olsson, 2014, Exact ab initio transport coefficients in bcc Fe-X (X=Cr, Cu, Mn, Ni, P, Si) dilute alloys, *Phys. Rev. B*, Vol. 90, 104203.
11. Martin, G., and P. Bellon, 1997, in: Ehrenreich H, Spaepen F, (Eds.), *Driven alloys, Solid State Physics - Advances in Research and Applications*, Vol. 50, Elsevier Academic Press Inc., San Diego, pp. 189-331.
12. Nastar, M., and F. Soisson, 2012, Atomistic modeling of phase transformations: Point-defect concentrations and the time-scale problem, *Phys. Rev. B*, Vol. 86, 220102(R).
13. Schmelzer, J.W.P, 2004, A new approach to nucleation theory and its application to phase formation processes in glass-forming melts, *Physics and Chemistry of Glasses*, Vol. 45, pp. 116-120.
14. Schmelzer, J.W.P., A.S. Abyzov, and J. Moller, 2004, Nucleation versus spinodal decomposition in phase formation processes in multicomponent solutions, *The Journal of Chemical Physics*, Vol. 121, pp. 6900-6917.
15. Schmelzer, J.W.P., A.R. Gokhman, and V.M. Fokin, 2014, Dynamics of first-order phase transitions in multicomponent systems: a new theoretical approach, *Journal of Colloid and Interface Science*, Vol. 272, pp. 109-133.
16. Slezov, V.V. 2009, *Kinetics of First Order Phase Transitions*.

17. Wells, P.B., T. Yamamoto, B. Miller, T. Milot, J. Cole, Y. Wu, and G.R. Odette, 2014, Evolution of manganese–nickel–silicon-dominated phases in highly irradiated reactor pressure vessel steels, *Acta Materialia*, Vol. 80, pp. 205-219.

18. <Integrity of reactor pressure vessels in nuclear power plants_assessment of irradiation embrittlement effects in reactor pressure vessels steels.pdf>.

19. Ke, H., P. Wells, L. Barnard, G.R. Odette, and D. Morgan, Cluster dynamics modeling of Mn-Ni-Si precipitates in low-Cu reactor pressure vessel steels, in preparation.

20. Irmer, V., and M. Feller-Kniepmeier, 1972, Diffusion of manganese in a-iron single crystals of different purity, *Journal of Physics and Chemistry of Solids*, Vol. 33, pp. 2141-2148.

21. Hirano, K., M. Cohen, and B.L. Averbach, 1961, Diffusion of nickel into Iron, *Acta Metallurgica*, Vol. 9, pp. 440-445.

22. Borg, R.J, 1970, Diffusion in α-Fe-Si Alloys, *Journal of Applied Physics*, Vol. 41, p. 5193.

23. Jiao, Z., and G.S. Was, 2011, Segregation behavior in proton- and heavy-ion-irradiated ferritic-martensitic alloys, *Acta Materialia*, Vol. 59, pp. 4467-4481.

24. Miller, M.K., K.A. Powers, R.K. Nanstad, and P. Efsing, 2013, Atom probe tomography characterizations of high nickel, low copper surveillance RPV welds irradiated to high fluences, *Journal of Nuclear Materials*, Vol. 437, pp. 107-115.

25. Edmondson, P.D., M.K. Miller, K.A. Powers, and R.K. Nanstad, 2016, Atom probe tomography characterization of neutron irradiated surveillance samples from the R. E. Ginna reactor pressure vessel, *Journal of Nuclear Materials*, Vol. 470, pp. 147-154.